Journal of Bio- and Tribo-Corrosion (2026) 12:69
https://doi.org/10.1007/s40735-026-01115-y

Effect of Cobalt Addition on Austenite Formation and Corrosion Behavior in Pulsed Nd:YAG Laser-Welded Super Duplex Stainless Steel UNS S32750

Bruna B. Seloto[1] · Mirko Pigato[2] · Claudio Gennari[2] · Irene Calliari[2] · Vicente A. Ventrella[1]

Received: 12 September 2025 / Revised: 6 January 2026 / Accepted: 24 January 2026 / Published online: 3 March 2026

Abstract

This study evaluates cobalt addition by electrodeposition on the microstructure and corrosion behavior of pulsed Nd:YAG laser-welded UNS S32750 SDSS. Four conditions Co_1, Co_2, Co_3 and Co_4, containing 3.3, 5.0, 7.5, and 11.0 wt% Co on the weld surface were analyzed by SEM/EDS, and cyclic polarization was performed in 3.5 wt% NaCl at 25 °C and 70 °C. Increasing Co promoted austenite formation in the fusion zone, and Co3 (7.5 wt% Co) showed the phase balance closest to the base metal, whereas the HAZ remained predominantly ferritic in all cases. At 25 °C, the curves exhibited a similar passive plateau and a highly restrictive hysteresis loop, with no measurable differences in localized corrosion resistance within the experimental scatter. At 70 °C, all welded conditions showed poor repassivation, with $E_{\mathrm{repassivation}}$ close to E_{corr}, indicating the weld as the critical site for localized corrosion and a secondary Co effect. EDS line scans showed a systematic decrease in the detected Cr and Mo signals with increasing Co, with Co_4 presenting the lowest intensities.

Keywords Super duplex stainless steel · Pulsed Nd:YAG laser welding · Cobalt electrodeposition · Austenite · Cyclic polarization

1 Introduction

Super duplex stainless steels (SDSS) are widely used in aggressive environments, such as offshore structures, chemical industries, pulp and paper facilities, and oil and gas systems, due to their high mechanical strength combined with excellent resistance to localized corrosion [1, 2]. These properties result from both their chemical composition, rich in Cr, Mo, N, and Ni, and their balanced biphasic microstructure of ferrite and austenite. This microstructure provides mechanical robustness and promotes the formation of a stable passive film in chloride-containing environments, thereby minimizing internal galvanic effects related to pitting corrosion [3–5]. However, phase balance and the associated corrosion performance are susceptible to the thermal cycles imposed during welding processes [5–7]. Previous studies have shown that different welding techniques, including conventional processes such as TIG/GTAW, can alter the ferrite–austenite balance and promote the precipitation of deleterious phases, such as sigma, chi, and chromium nitrides. These effects depend on heat input and exposure time within critical temperature ranges [1, 8].

Laser welding, particularly using pulsed Nd: YAG sources, has attracted increasing attention for joining SDSS due to its high energy density, low total heat input, and narrow heat-affected zone [9, 10]. However, the high heating and cooling rates associated with pulsed laser welding

✉ Bruna B. Seloto
b.seloto@unesp.br

Mirko Pigato
mirkopigato@gmail.com

Claudio Gennari
claudio.gennari@unipd.it

Irene Calliari
irene.calliari@unipd.it

Vicente A. Ventrella
vicente.ventrella@unesp.br

[1] Mechanical Engineering Department, São Paulo State University - UNESP, Campus of Ilha Solteira, São Paulo, Brazil

[2] Department of Industrial Engineering, University of Padova - UNIPD, Padova, Italy

promote non-equilibrium solidification conditions. These conditions frequently lead to ferrite-rich fusion zones [11, 12]. Such microstructural changes can significantly impair corrosion resistance, especially at elevated temperatures, where passive film stability becomes more critical [13, 14]. Such microstructural changes can significantly impair corrosion resistance, especially at elevated temperatures, where passive-film stability becomes more critical.Similar effects of thermal history on microstructural evolution and corrosion behavior have been reported in welded and heat-affected steels, in which rapid heating and cooling modify phase balance and local chemistry, directly affecting corrosion morphology and degradation mechanisms [15–17].

Phase imbalance between austenite and ferrite remains the main challenge in welding duplex stainless steels [7]. According to the literature, an austenite volume fraction below 25% renders SDSS unsuitable for most industrial applications [1, 2].

To control phase balance during laser welding of duplex stainless steels (DSS), several studies have applied post-weld heat treatments [11, 18], pre-weld heat treatments [19], or the addition of austenite-stabilizing elements, such as nickel and nitrogen [20, 21]. Da Cruz Junior et al. investigated the influence of introducing a 30 µm thick electrolytic nickel foil as an additive material during pulsed Nd: YAG laser welding of SDSS. The authors achieved a balanced microstructure with approximately 50% austenite and 50% ferrite in the fusion zone [22]. In a complementary approach, Videira et al. showed that nitrogen addition during hybrid GTAW–pulsed Nd: YAG laser welding increased the austenite fraction and improved corrosion resistance in UNS S32750 welded joints [23]. In different steel grades, similar strategies have been employed to tailor microstructure and improve corrosion performance, including compositional adjustments and thermal control, particularly under sour or high-temperature environments [17].

Although the influence of austenite-stabilizing alloying elements, such as Ni and N, on the ferrite–austenite balance and corrosion resistance of duplex stainless steels is well documented in welding and metallurgical literature, most studies focus on conventional processes or approaches based on commercial filler metals, modified shielding atmospheres, or global heat treatments. In contrast, investigations addressing localized modification of fusion zone chemistry, particularly under pulsed Nd: YAG laser welding conditions, remain limited.

Moreover, although cobalt is recognized as an alloying element with potential austenite-stabilizing effects in Fe–Cr–Ni systems [23], its role in the extremely rapid thermal cycles characteristic of pulsed laser welding remains insufficiently explored. Under such conditions, minor compositional variations can produce markedly different microstructural and electrochemical responses.

In this context, the effect of controlled cobalt addition, introduced through surface electroplating, on the microstructure and localized corrosion behavior of pulsed Nd: YAG laser-welded joints of UNS S32750 super duplex stainless steel was systematically investigated. The cobalt content was correlated with ferrite–austenite balance, phase microchemistry, and passive film stability. While cobalt addition increases austenite formation in the fusion zone, the corrosion behavior under aggressive conditions is dominated by the ferrite-rich weld microstructure rather than by cobalt content.

2 Materials and Methods

2.1 Welding Parameters and Cobalt Electrodeposition Process

The SDSS UNS S32750 plates, 15 mm x 50 mm x 2 mm, were used for experimental work, as shown in Fig. 1. The chemical composition of the material is shown in Table 1.

Pulsed Nd:YAG laser welding was carried out using a Nd: YAG laser source (model UW 150 A, United Winners) with a nominal power of 150 W and a maximum pulse energy of 80 J. The system was equipped with a CCD camera for

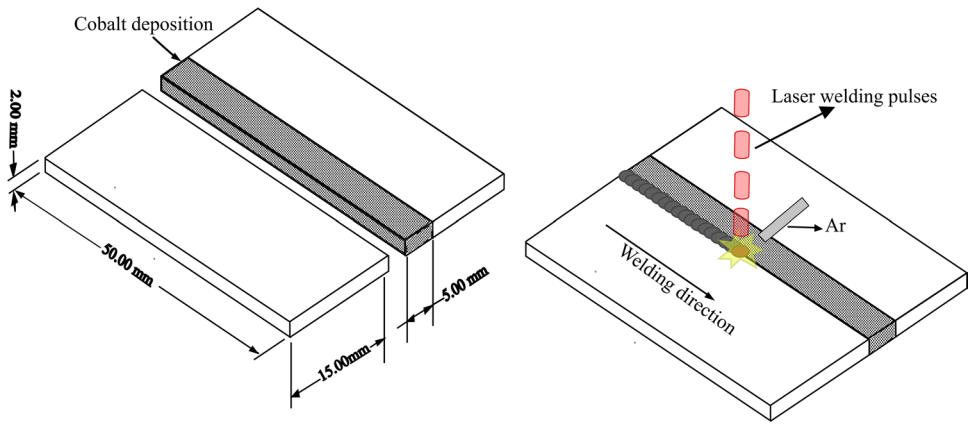

Fig. 1 Schematic representation of the pulsed Nd:YAG welding process

Table 1 Chemical composition of UNS S32750 (in wt%)

Base metal	C	Si	Mn	Cr	Ni	Mo	S	*P*	*N*
UNS S32750	0.018	0.290	0.630	25.610	6.970	3.840	0.003	0.022	0.269

Table 2 Welding parameters and conditions chosen

Pulse duration	Frequency	Peak power	Welding speed	Shielding gas
7 ms	9 Hz	2 kW	1 mm/s	20 L/min

process monitoring. In addition to the laser source, the experimental setup included a shielding gas supply system and a specimen holding table. The table movement was controlled by an Arduino-based system, allowing the welding speed to be regulated in a single direction.

The key process parameters for the weld samples Co_1, Co_2, Co_3, and Co_4, including pulse energy, pulse extent, repetition rate, and table speed, are listed in Table 2. They were kept constants for all samples. Also, argon gas at about 20 L/min is used near the top of the weld to prevent oxidation of the weld samples. The parameter process was obtained by performing sets of trial run experiments.

Cobalt electrodeposition was performed on the edge of one UNS S32750 duplex stainless-steel sheet, while the other sheet remained uncoated, resulting in a coated area of 650 mm². The process was carried out using a direct-current power supply and mechanical stirring of an electrolyte containing 31.2 g of $CoSO_4 \cdot 7\ H_2O$ 2 g of NaCl, and 7.6 g of H_3BO_3 dissolved in 100 mL of deionized water. Electrodeposition was conducted at room temperature with a current density of 3.7 A/dm², using an inert platinum electrode.

2.2 Surface and Microstructural Analysis

Each weld bead was divided into three sections, cut transversely to the weld. These segments were then sanded using sandpaper ranging from P-120 to P-3000 grit, and the samples were polished with 1 µm and 0.5 µm alumina suspensions. Subsequently, they were rinsed in distilled water and etched with a modified Behara reagent, consisting of 20 mL of HCl, 80 mL of H_2O, 1 g of $K_2S_2O_5$, and 2 g of NH_4HF_2.

A series of preliminary tests was conducted to determine the required cobalt amount to achieve the target austenite content. Once the appropriate cobalt layer thickness was established for each austenite level, electrodeposition was performed. The coating thickness was measured using a digital external micrometer with a measuring range of 0–25 mm, a resolution of 0.001 mm – Mitutoyo 293-244-30.

The surface microstructures were analyzed using an optical microscope (Fortel IM100) and a scanning electron microscope (SEM) model EVO LS15 (Zeiss), equipped with energy-dispersive X-ray spectroscopy (EDS). Chemical composition was determined by EDS analysis of the weld bead surface in different regions of the fusion zone to quantify and evaluate cobalt distribution. The samples were also examined under the optical microscope, and six micrographs were taken from each section. Each image was binarized in ImageJ to quantify the volumetric fractions of austenite and ferrite.

2.3 Electrochemical Measurements

Cyclic potentiodynamic polarization (Tafel) tests were performed at 25 °C and 70 °C using a Gamry Interface 1010E potentiostat. The measurements followed the procedures described in ASTM G61. The electrolyte consisted of an aqueous 3.5 wt% NaCl solution, used under naturally aerated conditions.

Before polarization, the open circuit potential (OCP) was monitored for 30 min to ensure stabilization. The polarization scans started at −0.1 V vs. the stabilized OCP, including the free corrosion region. A scan rate of 0.167 mV/s was applied. The anodic scan was reversed when the current density reached 5 mA/cm², in accordance with the standard.

The samples were mounted in a Teflon sample holder (AMEL). To prevent crevice corrosion, the exposed working area was defined using adhesive tape with circular openings, resulting in a circular exposed area of 12 mm². This area included both the fusion zone and the adjacent base material.

A platinum electrode served as the counter electrode, and a saturated calomel electrode (SCE) as the reference electrode. For measurements conducted at 70 °C, the reference electrode was separated from the main electrolyte using a Luggin capillary. This configuration ensured that the electrolyte surrounding the reference electrode remained below 30 °C, preventing thermal degradation or instability. Each test was repeated twice to confirm reproducibility.

3 Results and Discussion

3.1 Macro – and Microstructural Results

Figure 2a shows the top surface of the weld bead for sample Co_1. The region was sectioned, metallographically prepared, and analyzed by SEM to evaluate the weld-bead geometry and dimensions, as shown in Fig. 2b. Since all samples (Co_1 to Co_4) exhibited the same weld bead geometry, only the weld bead corresponding to condition Co_1 is presented. Weld bead geometry depends on the

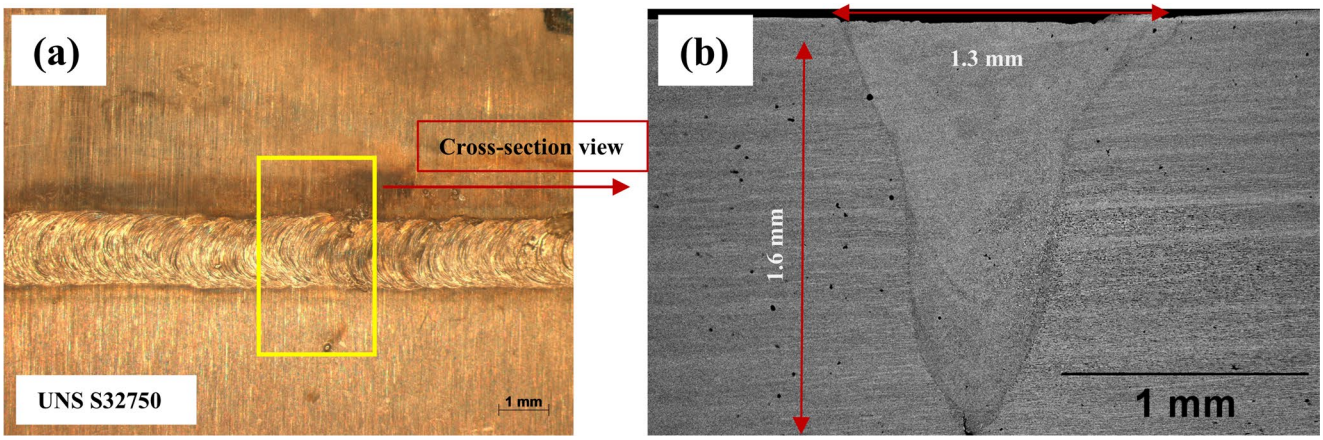

Fig. 2 **a** Top surface view of the weld bead for sample Co_1 **b** transverse cross-section of the weld bead for sample Co_1

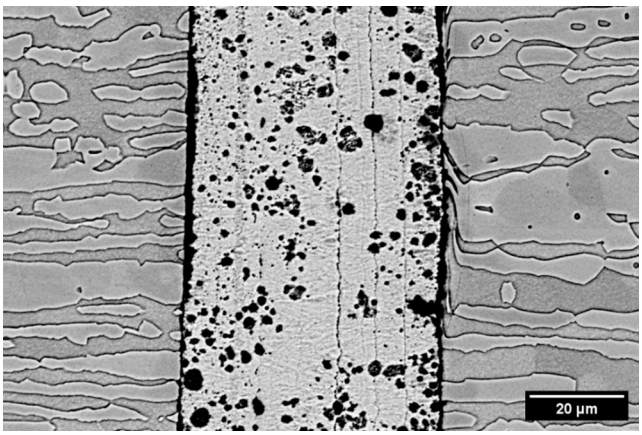

Fig. 3 Scanning electron microscopy (SEM) image of the deposited layer of sample Co_4

welding parameters and process mode, which were kept constant throughout the experiments.

As shown in Fig. 2a, the weld bead is clean, with minimal spatter and no surface cracks. In Fig. 2b, the bead presents no porosity or cracks. The bead has a funnel-like shape (1.3 mm wide and 1.6 mm deep) with high penetration, which is characteristic of keyhole laser welding and a narrow Heat-Affected Zone (HAZ) [12].

The cobalt deposited surface exhibited satisfactory adhesion, uniformity, and a matte silver appearance. To evaluate the coating quality, EDS analyses were performed on the layer of each sample, yielding 94%, 92.8%, 98.76%, and 98.55% cobalt content for samples Co_1, Co_2, Co_3, and Co_4, respectively. Figure 3 shows the SEM image of the electrodeposited layer.

The high cooling rates associated with pulsed Nd:YAG laser welding promote a pronounced phase imbalance in the fusion zone, characterized by a predominance of ferrite and limited austenite formation [25]. As shown in Fig. 4a, the base metal exhibits a nearly balanced microstructure with approximately 50% austenite and 50% ferrite. In contrast, in the fusion zone (Fig. 4b), austenite is mainly restricted to grain boundaries, due to the predominance of ferrite in the fusion zone, which is attributed to the highly unbalanced solidification conditions imposed by pulsed Nd:YAG laser welding, in which δ-ferrite forms first due to its greater stability at elevated temperatures. Austenite formation occurs via $\delta \rightarrow \gamma$ solid-state transformation during cooling;

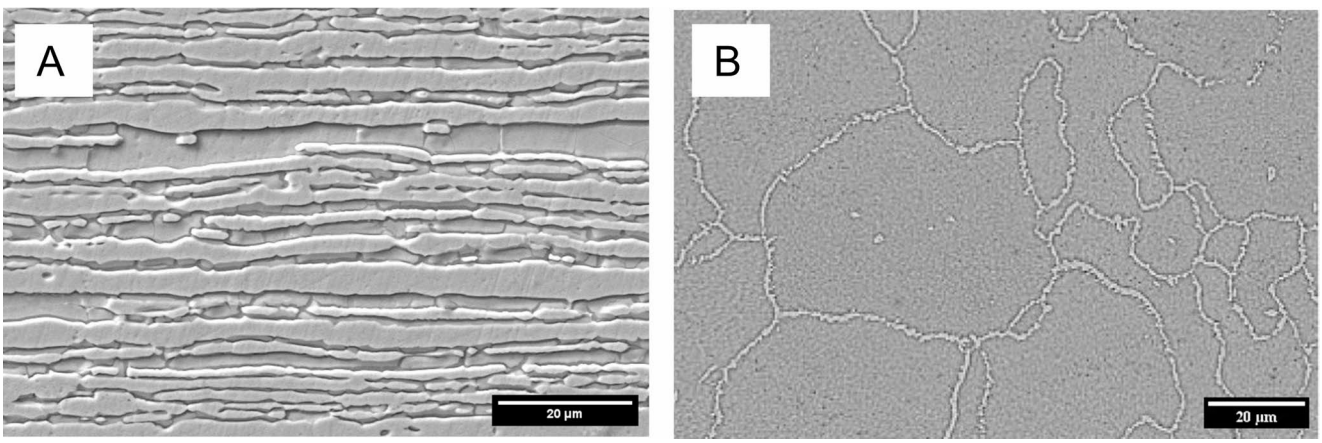

Fig. 4 **a** SEM image of UNS S32750 super duplex stainless steel. On the right – **b** SEM image of the fusion zone after pulsed Nd:YAG welding

however, the high cooling rates restrict element diffusion, limiting austenite growth primarily to grain boundaries.

Figure 5a, b shows the transition region of sample Co_1 from the base metal to the fusion zone (FZ), with a narrow HAZ, characteristic of pulsed Nd: YAG laser welding. Three types of austenite (γ) are identified: grain boundary austenite (GBA), intergranular austenite (IGA), and Widmanstätten austenite (WA). An arrow highlights the formation of austenite (γ) in the lighter regions, while ferrite (δ) appears in the darker regions. The FZ exhibits a predominantly ferritic structure, consistent with observations in welds without cobalt addition. This is because δ-ferrite is the first phase to form upon solidification from the liquid state. The phase transformation sequence for super duplex stainless steels (SDSS) during welding can be summarized as: L→L + F→F→F + A, where F, L, $and\ A$ are ferrite, liquid and austenite, respectively [4].

In Fig. 5c–h, the WM extending from the grain boundaries becomes more evident. The results show that increasing cobalt content increases the austenite volume fraction, confirming cobalt's role as an austenite stabilizer. Cobalt expands the austenite field in the phase diagram, which increases the transformation temperature of δ → γ; thus, austenite has a greater opportunity to reorganize and grow in the rapid cooling of pulsed laser welding Nd: YAG. Consequently, cobalt promoted the δ → γ transformation near

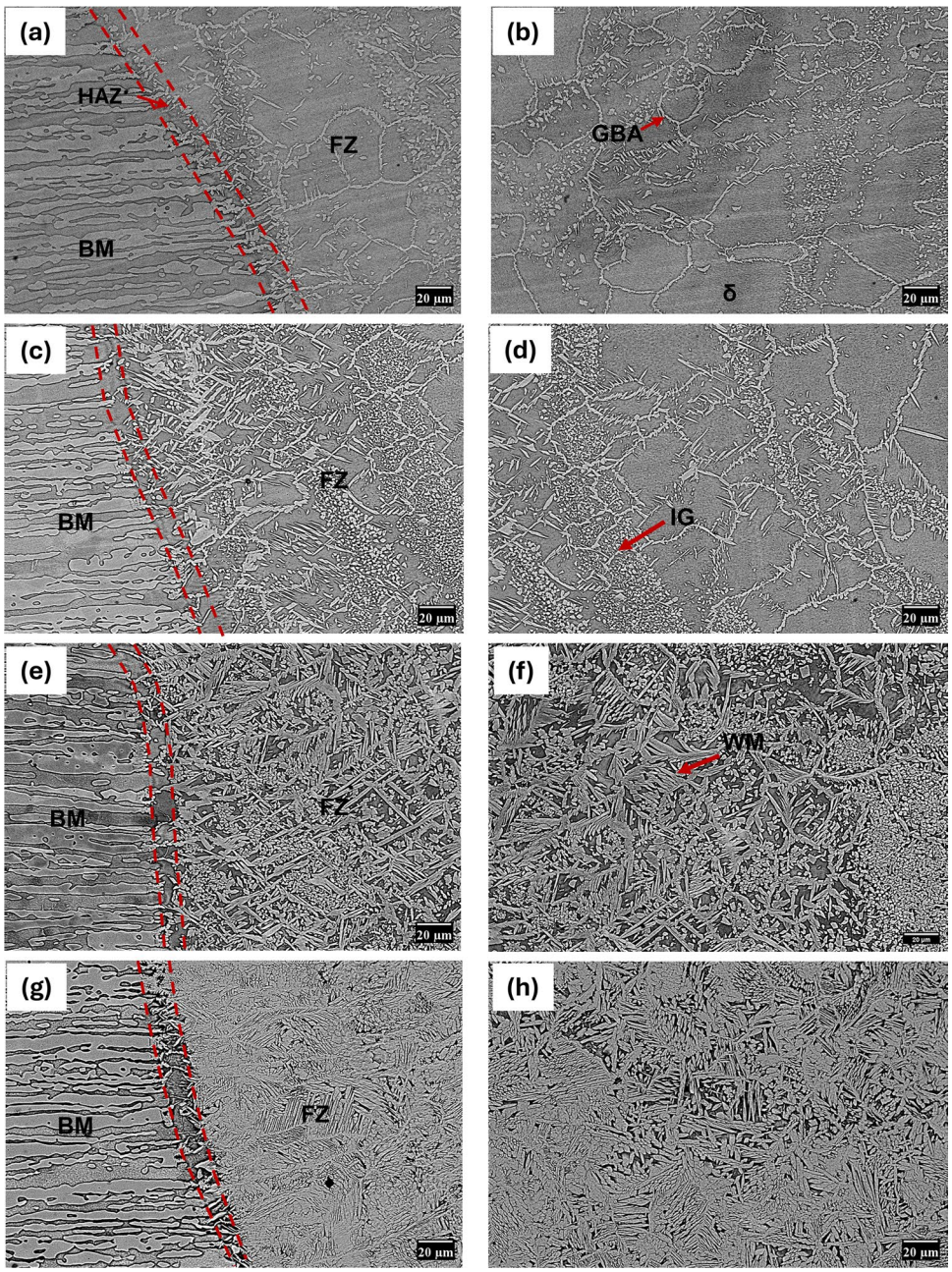

Fig. 5 SEM micrographs of samples Co_1–Co_4. Panels **A**, **C**, **E**, and **G** show the BM–FZ transition, while panels **B**, **D**, **F**, and **H** correspond to the FZ. Each pair (**A**, **B**), (**C**, **D**), (**E**, **F**), and (**G**, **H**) refers respectively to samples Co_1, Co_2, Co_3, and Co_4

Table 3 The deposited layer thicknesses, volumetric fractions of austenite and ferrite, and surface EDS results for each sample

Samples	Co thickness (μ m)	Vol% austenite	Vol% ferrite	EDS wt% Co (surface)
Co_1	21.3	23.8	76.2	3.3
Co_2	29.5	31.3	68.7	5.0
Co_3	43.0	43.5	57.7	7.5
Co_4	60.9	88.0	22.0	11.0

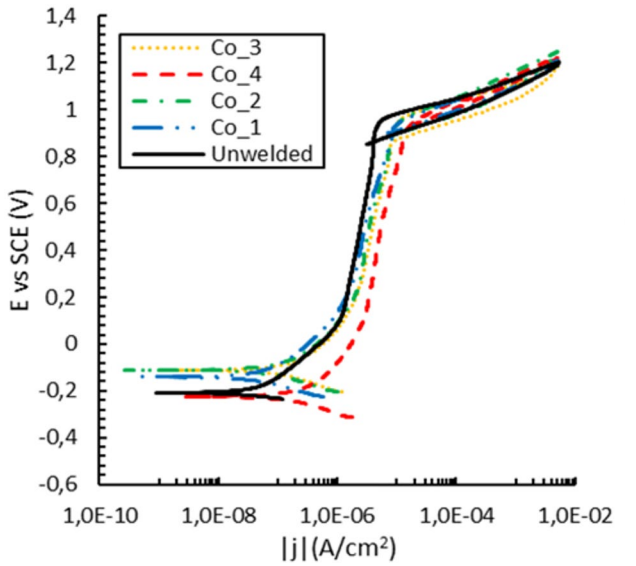

Fig. 6 Cyclic polarization in 3.5% NaCl solution at 25 °C for the welded samples

grain boundaries, increasing both the amount and size of WA within the FZ. Despite this austenite increase in the FZ, no such effect was observed in the HAZ, which remained predominantly ferritic, as shown in Fig. 5a, b, c, and f. This behavior can be attributed to the extremely rapid cooling in the HAZ, which limits cobalt diffusion and the δ → γ phase transformation [5]. Figure 5d the microstructural analysis reveals bands of intragranular IGA resulting from the reheating effect of overlapping laser pulses, which supplied the necessary thermal energy to trigger intragranular nucleation [23].

The quantitative analysis of austenite and ferrite volume fractions is presented in Table 3, together with the coating thickness and cobalt mass percentages obtained by EDS on the weld bead surface in the fusion zones of each sample. A clear trend is observed: greater coating thickness and higher cobalt content (measured by EDS) result in an increase in austenite content (quantified using ImageJ), reinforcing cobalt's γ-phase stabilizing effect. Sample Co3 exhibited the austenite fraction closest to that of the base metal, at 43.5%.

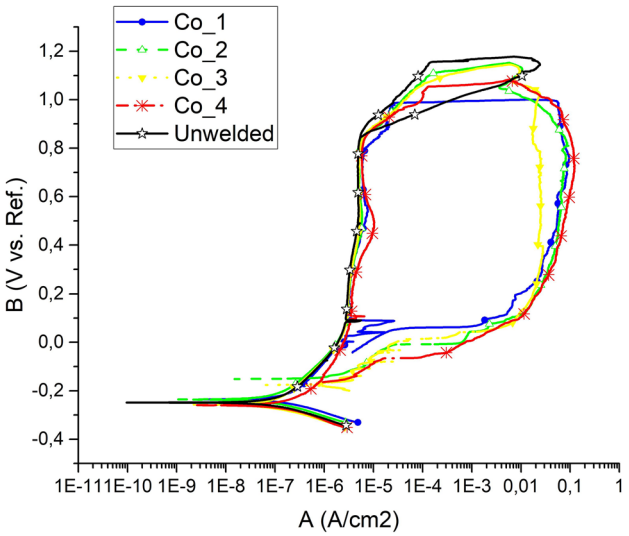

Fig. 7 Cyclic polarization in 3.5% NaCl solution at 70 °C for the welded samples

Table 4 Characteristic values of the polarization curves at 25 °C with varying cobalt content

Samples	I_{corr} (μ A/cm²)	E_{corr} (mV)	$E_{breakdown}$ (mV)	$E_{repassivation}$ (mV)
Co_1	0.10	−164	937	915
Co_2	0.15	−129	934	911
Co_3	0.27	−156	941	919
Co_4	0.37	−192	932	920
Unwelded	0.10	−187	930	921

Table 5 Characteristic values of the polarization curves at 70 °C with varying cobalt content

Samples	I_{corr} (μ A/cm²)	E_{corr} (mV)	$E_{breakdown}$ (mV)	$E_{repassivation}$ (mV)
Co_1	0.28	−245	850	80
Co_2	0.12	−235	853	−148
Co_3	0.19	−258	847	−173
Co_4	0.12	−256	851	−165
Unwelded	0.15	−247	853	842

3.2 Electrochemical Corrosion Behavior Analysis

Figures 6 and 7 show cyclic polarization curves in 3.5 wt% NaCl at 25 °C and 70 °C. Open-circuit potential (OCP) was monitored for 30 min before polarization until stabilization. The polarization scan was started at OCP−0.1 V to include the active corrosion region in the curves. Tables 4 and 5 summarize E_{corr}, I_{corr}, $E_{breakdown}$, and $E_{repassivation}$. All potential is reported in mV vs. SCE.

At 25 °C, all conditions show an apparent passive plateau and similar curve shapes. The passive-region current level and the passive range remain comparable across samples. The slight differences in $E_{breakdown}$ and $E_{repassivation}$

match this trend. Therefore, cobalt does not produce a measurable change in pitting resistance at 25 °C within the present scatter. Differences in I_{corr} suggest, at most, a minor effect on uniform dissolution at higher Co content. The repassivation observed during the backward scan demonstrates that the increase in current at a potential of 941 mV ($E_{breakdown}$) is associated with a transpassive phenomenon not correlated with the pitting corrosion. This behavior is attributed to the instability of the passive layer at high potentials, which leads to an enhanced dissolution rate of metallic ions through an increase in vacancies and a consequent rise in the ionic conductivity of the passive film [5] From Table 4 is possible note $E_{repassivation}$ are similar for all samples. It is typical for this grade of SDSS to display a highly restrictive or negligible hysteresis loop under cyclic polarization.

The $E_{breakdown}$ measured at 70 °C in 3.5% NaCl shifted to a less noble potential compared to that at 25 °C yet remained the same across all samples. At 70 °C, while in the bulk, Unwelded sample, the $E_{repassivation}$ once again corresponds to the $E_{brealdown}$ of the passive layer, with no signs of pits and with selective corrosion mainly affecting the ferritic phase, its grain boundaries, and the interphase interfaces (Fig. 7), in the welded samples, the $E_{\mathrm{repassivation}}$ remains consistently close to the free E_{corr}. This indicates that, under the tested conditions, the weld is always a weak point in terms of corrosion resistance, regardless of Co wt%. In the bulk sample, an additional increase in anodic current can be observed at approximately 1.2 V, likely associated with the oxygen evolution reaction. In contrast, for the welded samples, the change in slope of the curve at potential higher than the $E_{breakdown}$ occurs at lower voltages. In the Co_1 sample, in particular, a sharp increase in current is observed at 1000 mV, likely due to the propagation of stable pits. Passivity loses effectiveness at nearly identical potentials across the various samples, associated with a more defective passive layer, but above this potential, due to the reduced protection of the passive layer, pit propagation can be observed in the presence of welds.

In addition, at 70 °C, Co_1 shows a nearly horizontal segment at high anodic potentials. In this potential domain (≈ 1.0 V), the increase in anodic current can be influenced by oxygen evolution; oxygen bubbles formed near the surface may raise the apparent current density and promote passive-film disturbance, thus affecting the curve shape [19]. Bubble-related non-kinetic effects are known to convolute the electrochemical response in the oxygen evolution regime.

At 70 °C, the base metal exhibited no evidence of pitting. Given that $E_{repassivation}$ remained close to the $E_{breakdown}$, the corrosion was primarily confined to the ferritic phase, as shown in Fig. 8(Bulk). In contrast, all welded samples showed clear signs of pitting localized in the fusion zone, as illustrated in Fig. 8(Co_4) (see Fig. 8).

3.3 EDS Analysis

Figure 9a SEM micrograph indicating the EDS line-scan path (white line) across the weld region. Figure 9b shows a representative line-sum spectrum obtained by integrating the X-ray counts along the scan, highlighting the main detected elements. Figure 10 presents the EDS line-scan intensity Cr Kα profile, and Fig. 11 the EDS line-scan intensity of Mo Lα across the fusion zone (FZ), for comparison among conditions, the line-scan position was expressed as a normalized distance (0–1), where 0 and 1 correspond to the beginning and end of the scan line.

For each condition, the Cr Kα and Mo Lα signals are relatively uniform along the scan, with no pronounced local peaks. The main difference among conditions is a systematic shift in intensity level. The as-welded condition

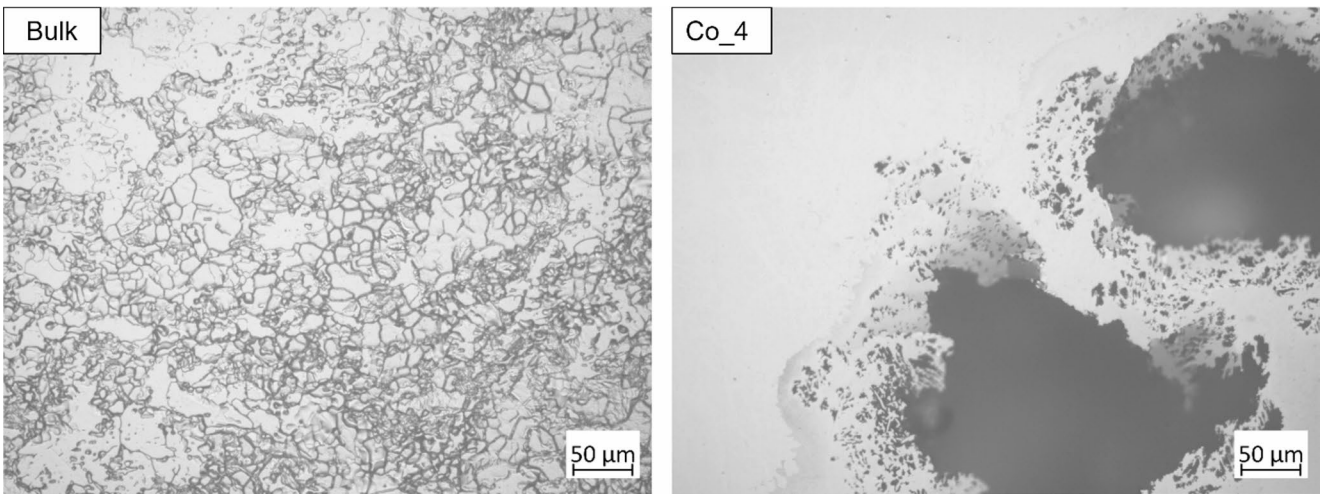

Fig. 8 Corroded surface of the bulk and Co_4 samples after the cyclic polarization at 70 °C in 3.5% of NaCl

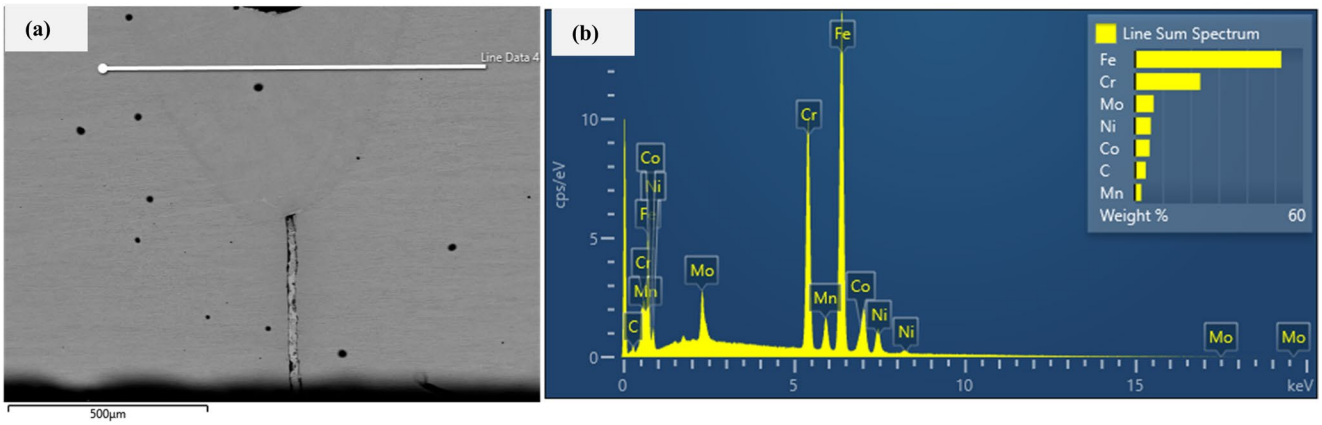

Fig. 9 **a** SEM micrograph from the EDS line-scan from sample Co_2 and **b** shows the line spectrum obtained

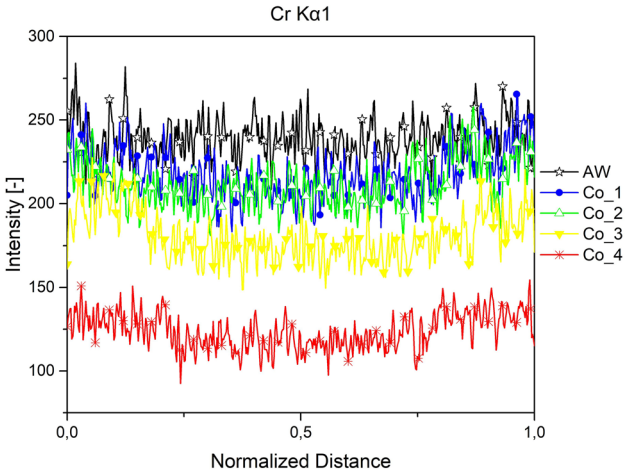

Fig. 10 Cr Kα1 intensity profile vs. normalized distance for all samples

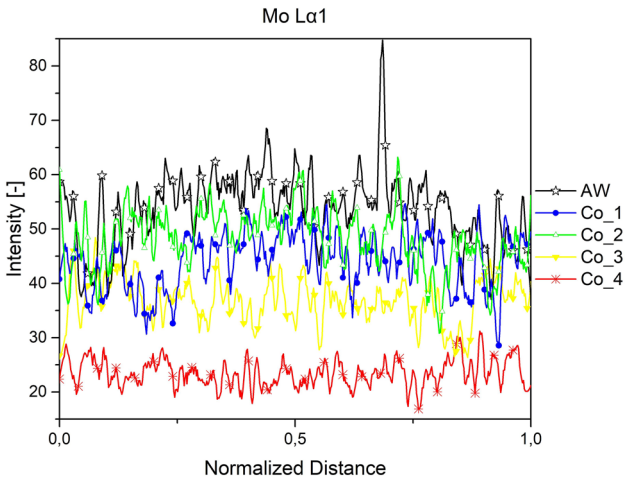

Fig. 11 Mo Lα1 intensity profile vs. normalized distance in all samples

without Co (AW) shows the highest Cr and Mo intensities. With increasing Co content, the detected Cr and Mo signals decrease, with Co4 showing the lowest levels.

Because EDS line scans provide X-ray counts rather than quantitative composition, the lower Cr/Mo intensities are interpreted as a relative decrease in detected signal under the acquisition conditions employed, not as direct evidence of absolute Cr/Mo depletion. X-ray intensity can be affected by matrix effects and attenuation within the analyzed volume. Accordingly, the line-scan profiles indicate that the FZ exhibits a less favorable Cr/Mo signal response across the Co series than in the AW condition, consistent with the chemical/structural heterogeneity typical of rapidly solidified weld metal.

At 70 °C, all welded conditions show poor repassivation, with $E_{\mathrm{repassivation}}$ close to E_{corr} and no relevant differences between Co_1 and Co_4. Therefore, the EDS line-scan trend is not used to explain variations in repassivation within the Co series. Instead, it supports the general conclusion that the FZ is a critical region for passive-film stability under aggressive conditions. In this context, the welded microstructure (ferrite-rich and heterogeneous) dominates the response, whereas any specific Co effect on repassivation, if present, is below the sensitivity of the present measurements.

4 Conclusion

This study evaluated the effect of controlled cobalt addition, introduced by surface electrodeposition, on the microstructure and corrosion behavior of pulsed Nd: YAG laser-welded UNS S32750 super duplex stainless steel.

The laser welds exhibited keyhole-like geometry and a narrow heat-affected zone under the fixed welding parameters. The fusion zone formed as a ferrite-rich structure due to rapid solidification, with austenite mainly restricted to grain boundaries. Increasing Co content promoted austenite

formation in the fusion zone, and Co3 provided the phase balance closest to the base metal among the tested conditions. No comparable effect was observed in the HAZ, which remained predominantly ferritic.

Cyclic polarization tests in 3.5 wt% NaCl showed that, at 25 °C, all conditions presented similar passive behavior and highly restrictive hysteresis, with no measurable differences in pitting resistance within the experimental scatter. At 70 °C, all welded conditions exhibited poor repassivation, with $E_{\mathrm{repassivation}}$ close to E_{corr}, whereas the base metal repassivated near $E_{\mathrm{breakdown}}$ and showed no evidence of stable pitting. These results indicate that the weld region is the critical site for localized corrosion at elevated temperature, largely independent of Co content within the investigated range.

EDS line scans showed a systematic decrease in the detected Cr and Mo signals across the Co series; however, since line scans report X-ray counts, this trend is discussed as a relative signal response consistent with weld heterogeneity rather than as direct evidence of absolute depletion.

Author Contributions Conceptualization and methodology: B.B. Seloto. Supervision: V.A. Ventrella, I. Calliari. Writing - original draft: B.B. Seloto. Data analysis: B.B.Seloto and M. Pigato. Experimental work: B.B. Seloto and M. Pigato in electrochemical tests. Writing and review & editing: all authors.

Funding The Article Processing Charge (APC) for the publication of this research was funded by the Coordenação de Aperfeiçoamento de Pessoal de Nível Superior - Brasil (CAPES) (ROR identifier: 00x0ma614). This study was partially financed by the Coordenação de Aperfeiçoamento de Pessoal de Nível Superior - Brasil (CAPES). Finance Code 001.

Data Availability Data are available from the corresponding author upon reasonable request.

Declarations

Conflict of interest The authors declare no competing interests.

References

1. Nilsson JO (1992) Super duplex stainless steels
2. Charles J (2008) Duplex stainless steels - a review after DSS '07 held in Grado. Steel Res Int 79:455–465. https://doi.org/10.1002/SRIN.200806153
3. Francis R, Byrne G (2021) Duplex Stainless Steels—Alloys for the 21st Century. Metals 11:836. https://doi.org/10.3390/MET11050836
4. Kang DH, Lee HW (2013) Study of the correlation between pitting corrosion and the component ratio of the dual phase in duplex stainless steel welds. Corros Sci 74:396–407. https://doi.org/10.1016/j.corsci.2013.04.033
5. Långberg M, Örnek C, Evertsson J et al (2019) Redefining passivity breakdown of super duplex stainless steel by electrochemical operando synchrotron near surface X-ray analyses. NPJ Mater Degrad 3(1):22. https://doi.org/10.1038/s41529-019-0084-3
6. Zhang Z, Qu S, Zhang Y et al (2025) Microstructure, mechanical properties, and corrosion resistance of DSS laser-welded joints. Weld World. https://doi.org/10.1007/s40194-025-01977-9
7. Lippold JC, Kotecki DJ (2005) Welding metallurgy and weldability of stainless steels. Wiley, Hoboken
8. Gandhi AD, Neikter M, Axelsson B et al (2025) Solution annealing of PBF-LB manufactured 2507 super duplex stainless steel: a computational thermodynamics approach. Weld World 2025:1–15. https://doi.org/10.1007/S40194-025-02264-3
9. Sivagurumanikandan N, Saravanan S, Sivakumar G, Raghukandan K (2018) Process window for nd:yag laser welding of super duplex stainless steel. J Russ Laser Res 39:575–584. https://doi.org/10.1007/s10946-018-9754-9
10. Bolut M, Kong CY, Blackburn J et al (2016) Yb-fibre laser welding of 6 mm duplex stainless steel 2205. Phys Procedia 83:417–425. https://doi.org/10.1016/J.PHPRO.2016.08.043
11. Ahmad GN, Singh NK, Tripathi BN et al (2023) Monitoring of thermo-cycles in fibre laser welding of duplex stainless steel 2205 sheets and its correlation with microstructures and mechanical properties. Mater Res Express 10:106517. https://doi.org/10.1088/2053-1591/AD0095
12. Guo S, Zou J, Xu J et al (2021) Multi-stage keyhole evolution in fiber laser welding: an experimental study and theoretical analysis. Results Phys 31:104943. https://doi.org/10.1016/J.RINP.2021.104943
13. Leiva-García R, Fernandes JCS, Muñoz-Portero MJ, García-Antón J (2015) Study of the sensitisation process of a duplex stainless steel (UNS 1.4462) by means of confocal microscopy and localised electrochemical techniques. Corros Sci 94:327–341. https://doi.org/10.1016/J.CORSCI.2015.02.016
14. Miranda-Pérez AF, Rodríguez-Vargas BR, Calliari I et al (2023) Corrosion resistance of GMAW duplex stainless steels welds. Materials 16:16. https://doi.org/10.3390/MA16051847
15. Sabzi M, Far SM, Dezfuli SM (2019) Effect of melting temperature on microstructural evolutions, behavior and corrosion morphology of Hadfield austenitic manganese steel in the casting process. Int J Miner Metall Mater 2018(12):1431–1438. https://doi.org/10.1007/S12613-018-1697-1
16. Sabzi M, Jafarian HR, Abdollahzadeh A et al (2025) Pulsed current gas tungsten arc welded joint of ASTM A105-AISI 316L steels: failure analysis and susceptibility to hydrogen embrittlement under slow strain rate tensile tests, and hydrogen sulfide corrosion. Results Eng 27:107055. https://doi.org/10.1016/J.RINENG.2025.107055
17. Sabzi M, Jozani AH, Zeidvandi F et al (2022) Effect of 2-mercaptobenzothiazole concentration on sour-corrosion behavior of API X60 pipeline steel: electrochemical parameters and adsorption

mechanism. Int J Min Metall Mater 2022 29(2):271–282. https://doi.org/10.1007/S12613-020-2156-3
18. Landowski M (2019) Influence of parameters of laser beam welding on structure of 2205 duplex stainless steel. Adv Mater Sci 19:21–31. https://doi.org/10.2478/ADMS-2019-0002
19. Cruz ALS, de Lima HMLF, Xavier ARV et al (2023) Comparative study of the influence of aging time at 850°C on the electrochemical behaviour of two cast super duplex stainless steel. Mater Res 26:e20230034. https://doi.org/10.1590/1980-5373-MR-2023-0034
20. Muthupandi V, Bala Srinivasan P, Seshadri SK, Sundaresan S (2003) Effect of weld metal chemistry and heat input on the structure and properties of duplex stainless steel welds. Mater Sci Eng A 358:9–16. https://doi.org/10.1016/S0921-5093(03)00077-7
21. Xia Y, Amatsu K, Miyasaka F, Mori H (2021) Effect of nitrogen on weldability and the microstructure in laser beam welding of duplex stainless steel. Miner Met Mater Ser. https://doi.org/10.1007/978-3-030-65253-1_17
22. da Cruz Junior EJ, Franzini OD, Calliari I, Ventrella VA (2019) Effects of nickel addition on the microstructure of laser-welded UNS S32750 duplex stainless steel. Metall Mater Trans A Phys Metall Mater Sci 50:1616–1618. https://doi.org/10.1007/s11661-019-05115-1
23. Videira AM, Mendes WR, Ventrella VA et al (2023) Increasing the corrosion resistance in the UNS S32750 super duplex steel welded joints through hybrid GTAW-laser welding and nitrogen. Materials 16(2):16: https://doi.org/10.3390/MA16020543
24. Shibuya M, Toda Y, Sawada K et al (2011) Effect of nickel and cobalt addition on the precipitation-strength of 15Cr ferritic steels. Mater Sci Eng A Mater Struct Prop Microstruct Process 528:5387–5393. https://doi.org/10.1016/J.MSEA.2011.03.088
25. Saravanan S, Sivagurumanikandan N, Raghukandan K (2021) Effect of process parameters in microstructural and mechanical properties of nd: YAG laser welded super duplex stainless steel. Mater Today Proc 39:1248–1253. https://doi.org/10.1016/J.MATPR.2020.04.101